

Article

# First-Principles Investigations on Structural and Elastic Properties of Orthorhombic TiAl under Pressure

Lili Liu <sup>1,2,\*</sup>, Xiaozhi Wu <sup>2,3</sup>, Rui Wang <sup>2</sup>, Xiangfei Nie <sup>1</sup>, Yelu He <sup>1</sup> and Xing Zou <sup>1</sup>

<sup>1</sup> Department of Physics, Chongqing Three Gorges University, Wanzhou 404100, China; niexf@tom.com (X.N.); 15215155968@139.com (Y.H.); 15696635836@163.com (X.Z.)

<sup>2</sup> Institute for Structure and Function, Chongqing University, Chongqing 401331, China; xiaozhiwu@cqu.edu.cn (X.W.); rwang@cqu.edu.cn (R.W.)

<sup>3</sup> College of Materials Science and Engineering, Chongqing University, Chongqing 400044, China

\* Correspondence: liulili0612@163.com

Academic Editors: Glen Deacon and Helmut Cölfen

Received: 1 March 2017; Accepted: 5 April 2017; Published: 13 April 2017

**Abstract:** The effects of pressure on the structural and elastic properties of orthorhombic TiAl are investigated using first-principles calculations based on density functional theory within the projector augmented wave method. The calculated lattice parameters at 0 GPa are in good agreement with the available experimental data. The pressure dependence of the normalized lattice parameters and the single crystal elastic constants are investigated. By the elastic stability criteria under pressure, it is found that orthorhombic TiAl is mechanically stable under pressure up to 100 GPa. The elastic moduli and Poisson's ratio under pressure up to 100 GPa are calculated using the Hill average method. The ductility/brittleness under pressure are evaluated, and a critical pressure for brittle-to-ductile transition is found to be 40 GPa. The elastic anisotropy and Debye temperature under different pressure are estimated from the calculations.

**Keywords:** orthorhombic TiAl; structural property; elastic property; pressure; first-principles

## 1. Introduction

Intermetallic alloys based on  $\gamma$ -TiAl are widely considered as promising high-temperature structural materials for aerospace and automotive applications because of their low density, high strength, and good high temperature resistances to creep, oxidation, and corrosion [1]. However, these alloys have the serious drawback of their low ductility that also results in their limited hot workability. One strategy to improve their ductility and hot workability is to employ a combination of alloying and heat treatments to encourage the formation of more ductile phases. Nevertheless, the strategy can also induce the formations of some lower symmetry ordered phases which are constituents of the microstructure [1–3]. As a significant constituent, the orthorhombic B19-TiAl phase is commonly observed in TiAl-based alloys [2–7].

Although some experiments have been reported with the aim of understanding the B19-TiAl phase, theoretical calculations are still rare. Using first-principles calculations, Nguyen-Manh and Pettifor [8,9] successfully investigated the structural phase transitions related to the B19-TiAl phase. Recently, Holec et al. [10] investigated the preferential site occupations of ternary elements in the B19-TiAl. Most recently, Wen et al. [11] investigated the structural stability and the elastic and mechanical properties of the B19-TiAl at ground state. However, to our knowledge, the influence of pressure on the structural, elastic, and mechanical properties of the B19-TiAl has not been reported so far.

In this work, we will use first-principles calculations to further investigate the structural, elastic, and mechanical properties of orthorhombic B19-TiAl under pressure. The rest of the manuscript is

organized as follows: the computational methodology is briefly described in Section 2; the pressure dependence of the structural, elastic, and mechanical properties is presented in Section 3, together with detailed discussions; the conclusions are finally drawn in Section 4.

## 2. Computational Methodology

Density functional theory-based first-principles calculations of orthorhombic B19-TiAl were performed using the projector augmented wave method [12] within the Perdew–Burke–Ernzerhof (PBE) generalized gradient approximations (GGA) [13,14], as implemented in the Vienna Ab initio Simulation Package (VASP) [15–17]. The  $3s^23p^63d^24s^2$  and  $3s^23p^1$  were treated as the valence electron configurations for Ti and Al, respectively. An energy cut-off or the plane wave basis set was set to 600 eV. The energy convergence threshold was  $10^{-6}$  eV. Special sampling points in the Brillouin zone were generated by the Monkhorst–Pack scheme [18], and a k-point mesh of  $11 \times 19 \times 11$  was used for the orthorhombic TiAl. Before calculating the elastic constants, the structures at the given pressure  $P$  were fully relaxed with respect to the volume, shape, and internal atomic positions until the atomic forces were less than  $0.01 \text{ eV}/\text{\AA}$  for a unit cell. The phonon dispersion calculations for the orthorhombic B19-TiAl were performed using a  $3 \times 4 \times 3$  supercell with 124 atoms and  $4 \times 5 \times 4$  k-points grid meshes for BZ integrations.

An orthorhombic crystal has nine independent elastic constants  $C_{11}$ ,  $C_{22}$ ,  $C_{33}$ ,  $C_{12}$ ,  $C_{13}$ ,  $C_{23}$ ,  $C_{44}$ ,  $C_{55}$ , and  $C_{66}$ . Starting from the optimized geometry of a unit cell at the given pressure, the elastic constants of the orthorhombic TiAl can be determined using the strain–stress relationship method embedded in the VASP. The elastic tensor is determined by performing six finite distortions of the lattice and deriving the elastic stiffness constants from the strain–stress relationship [19]. The elastic tensor is calculated both for rigid ions, as well as allowing for relaxation of the ions. The ionic contributions are determined by inverting the ionic Hessian matrix and multiplying with the internal strain tensor [20–23]. The final elastic stiffness constants include both the contributions for distortions with rigid ions and the contributions from the ionic relaxations.

Once the single crystal elastic constants are obtained, we could determine the isotropic bulk modulus  $B$  and shear modulus  $G$ . In practice, these quantities are commonly estimated using the Hill average method, in which the effective elastic moduli are the arithmetic averages of Voigt and Reuss bounds [24]. For the specific case of orthorhombic crystals, the Voigt bounds on bulk ( $B_V$ ) and shear ( $G_V$ ) moduli are defined as [25]

$$\begin{aligned} B_V &= (C_{11} + 2C_{12} + 2C_{13} + C_{22} + 2C_{23} + C_{33})/9, \\ G_V &= (C_{11} - C_{12} - C_{13} + C_{22} - C_{23} + C_{33} + 3C_{44} + 3C_{55} + 3C_{66})/15. \end{aligned} \quad (1)$$

The Reuss bounds on bulk ( $B_R$ ) and shear ( $G_R$ ) moduli are defined as [26]

$$\begin{aligned} B_R &= \chi [C_{11}(C_{22} + C_{33} - 2C_{23}) + C_{22}(C_{33} - 2C_{13}) - 2C_{33}C_{12} \\ &\quad + C_{12}(2C_{23} - C_{12}) + C_{13}(2C_{12} - C_{13}) + C_{23}(2C_{13} - C_{23})]^{-1}, \\ G_R &= 15 \{ 4 [C_{11}(C_{22} + C_{33} + C_{23}) + C_{22}(C_{33} + C_{13}) + C_{33}C_{12} - C_{12}(C_{23} + C_{12}) \\ &\quad - C_{13}(C_{12} + C_{13}) - C_{23}(C_{13} + C_{23})] / \chi + 3 (C_{44}^{-1} + C_{55}^{-1} + C_{66}^{-1}) \}^{-1}, \\ \chi &= C_{13}(C_{12}C_{23} - C_{13}C_{22}) + C_{23}(C_{12}C_{13} - C_{23}C_{11}) + C_{33}(C_{11}C_{22} - C_{12}^2). \end{aligned} \quad (2)$$

The Hill averages of bulk ( $B$ ) and shear ( $G$ ) moduli are obtained by [24]

$$\begin{aligned} B &= (B_V + B_R)/2, \\ G &= (G_V + G_R)/2. \end{aligned} \quad (3)$$

The effective moduli can be used to calculate the Young's modulus ( $E$ ) and Poisson's ratio ( $\nu$ ) by

$$\begin{aligned} E &= 9BG/(3B + G), \\ \nu &= (3B - 2G)/(6B + 2G). \end{aligned} \quad (4)$$

In addition, the elastic anisotropy and Debye temperature can be estimated in terms of the above elastic constants and isotropic moduli. The single crystal shear anisotropy factors  $A_{\{100\}}$  in  $\{100\}$  planes,  $A_{\{010\}}$  in  $\{010\}$  planes, and  $A_{\{001\}}$  in  $\{001\}$  planes are defined as [27]

$$\begin{aligned} A_{\{100\}} &= 4C_{44}/(C_{11} + C_{33} - 2C_{13}), \\ A_{\{010\}} &= 4C_{55}/(C_{22} + C_{33} - 2C_{23}), \\ A_{\{001\}} &= 4C_{66}/(C_{11} + C_{22} - 2C_{12}). \end{aligned} \quad (5)$$

The deviation of  $A_{\{100\}}$  and  $A_{\{001\}}$  from one is a measure of the shear anisotropy. The percentage anisotropy in compressibility ( $A_B$ ) and shear ( $A_G$ ) is defined as [28]

$$\begin{aligned} A_B &= (B_V - B_R)/(B_V + B_R), \\ A_G &= (G_V - G_R)/(G_V + G_R). \end{aligned} \quad (6)$$

A zero value of  $A_B$  and  $A_G$  corresponds to elastic isotropy, while a value of 100% corresponds to the largest possible anisotropy. The universal anisotropy index ( $A^U$ ) is defined as [29]

$$A^U = B_V/B_R + 5G_V/G_R - 6. \quad (7)$$

A nonzero value of  $A^U$  is a measure of the anisotropy. The Debye temperature ( $\Theta_D$ ) is calculated as [30]

$$\Theta_D = (h/k)[(3n/4\pi)(N_A\rho/M)]^{1/3}V_m, \quad (8)$$

where  $h$  is the Plank's constant,  $k$  is Boltzmann's constant,  $n$  is the number of atoms per unit cell,  $N_A$  is Avogadro's number, and  $\rho$  is the mass density of the crystal.  $V_m$  is the average elastic wave velocity, which is given by

$$V_m = \left[ \left( 1/V_l^3 + 2/V_t^3 \right) / 3 \right]^{-1/3}, \quad (9)$$

where  $V_l$  and  $V_t$  correspond to the longitudinal and transverse elastic wave velocities, which are given by [31]

$$\begin{aligned} V_l &= [(3B + 4G)/3\rho]^{1/2}, \\ V_t &= (G/\rho)^{1/2}. \end{aligned} \quad (10)$$

### 3. Results and Discussion

The orthorhombic B19-TiAl has Pmma space group, and its crystal structure is shown in Figure 1. The experimental and theoretical structural parameters are presented in Table 1. Note that the present lattice parameters and elastic constants are obtained by using the method of Wen et al. [11]. From the selected-area electron diffraction patterns, the lattice parameters were estimated by Abe et al. [2] to be  $a = 4.5 \text{ \AA}$ ,  $b = 2.8 \text{ \AA}$ , and  $c = 4.9 \text{ \AA}$ , and by Ducher et al. [5] to be  $a = 4.65 \text{ \AA}$ ,  $b = 2.828 \text{ \AA}$ , and  $c = 4.94 \text{ \AA}$ , respectively. In the unit cell, there are two Ti and two Al atoms at 2e (1/4, 0, 5/6) and 2f (1/4, 1/2, 1/3) Wyckoff positions, respectively [5]. In the present study, the lattice parameters of the orthorhombic TiAl at 0 GPa are calculated to be  $a = 4.632 \text{ \AA}$ ,  $b = 2.863 \text{ \AA}$ , and  $c = 4.895 \text{ \AA}$ , which are in good agreement with the corresponding experimental values [2,5]. Ti and Al atoms occupy the respective Wyckoff positions 2e (1/4, 0, 0.83983) and 2f (1/4, 1/2, 0.33919) in the theoretically optimized unit cell, which agree with the respective experimental values [5].

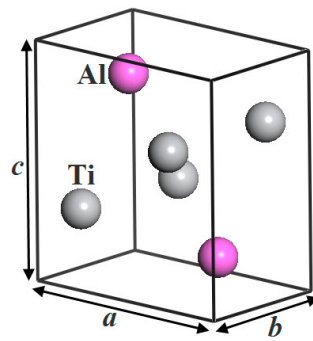


**Figure 1.** The orthorhombic structure of B19-TiAl.

**Table 1.** The lattice parameters ( $a$ ,  $b$ ,  $c$ ) and atomic Wyckoff positions ( $x$ ,  $y$ ,  $z$ ) of the orthorhombic TiAl.

Method	Lattice Parameter (Å)	Atom (Wyckoff)	Atomic Coordinates		
			$x$	$y$	$z$
Exp. [2]	$a = 4.50, b = 2.80, c = 4.90$				
Exp. [6]	$a = 4.65, b = 2.828, c = 4.94$	Ti (2e)	1/4	0	5/6
		Al (2f)	1/4	1/2	1/3
Present	$a = 4.632, b = 2.863, c = 4.895$	Ti (2e)	1/4	0	0.83983
		Al (2f)	1/4	1/2	0.33919

Figure 2 shows the pressure-dependent parameters  $a/a_0$ ,  $b/b_0$ ,  $c/c_0$ ,  $V/V_0$ ,  $a/b$ , and  $c/b$  of the orthorhombic TiAl, where  $a_0$ ,  $b_0$ ,  $c_0$ , and  $V_0$  are the equilibrium lattice constants and primitive cell volume at 0 GPa. In Figure 2a, the normalized lattice parameters and cell volume decrease with increasing pressure. By fitting these zero temperature theoretical data under different pressure with a second-order polynomial, we obtain the following relational expressions:

$$\begin{aligned}
 a/a_0 &= 0.99561 - 2.20 \times 10^{-3}P + 9.38330 \times 10^{-6}P^2, \\
 b/b_0 &= 0.99580 - 1.92 \times 10^{-3}P + 7.68101 \times 10^{-6}P^2, \\
 c/c_0 &= 0.99689 - 2.03 \times 10^{-3}P + 8.05396 \times 10^{-6}P^2, \\
 V/V_0 &= 0.98432 - 5.74 \times 10^{-3}P + 2.62120 \times 10^{-5}P^2.
 \end{aligned}
 \tag{11}$$

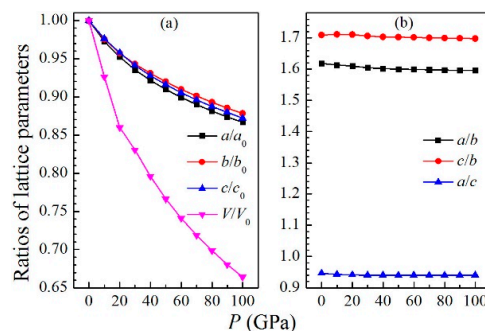


**Figure 2.** Pressure dependence of the normalized parameters (a)  $a/a_0$ ,  $b/b_0$ ,  $c/c_0$ , and  $V/V_0$  and (b) the ratios  $a/b$ ,  $c/b$ , and  $a/c$  of the orthorhombic TiAl.

The goodness of fit for the equations are 0.996 for  $a/a_0$ , 0.996 for  $b/b_0$ , 0.998 for  $c/c_0$ , and 0.993 for  $V/V_0$ . From the first-order coefficients of these function expressions, one can find that when the pressure increases, the normalized lattice parameter  $a/a_0$  decreases most quickly, followed by  $c/c_0$ ;  $b/b_0$  decreases most slowly, indicating that the  $a$  axis is most easily compressed, while the  $b$  axis most difficultly. In Figure 2b, the ratios  $a/b$ ,  $c/b$ , and  $a/c$  decrease slightly with increasing pressure.

Table 2 lists the calculated results of the single crystal elastic constants of the orthorhombic TiAl under pressure up to 100 GPa. All of the computed elastic constants have been corrected according to the procedure described by Mahmoud et al. [32]. It can be found that (except for  $C_{44}$  and  $C_{55}$ ) other elastic constants increase monotonously with increasing pressure. The  $C_{11}$ ,  $C_{22}$ , and  $C_{33}$  are susceptible to the pressure, while the  $C_{12}$ ,  $C_{13}$ ,  $C_{23}$ , and  $C_{66}$  have little variations under pressure. As the pressure increases, the  $C_{44}$  and  $C_{55}$  firstly increase and then start to decrease after 70 GPa and 90 GPa, respectively. Although no available experimental and theoretical data are employed to cross-check the present results, these results can provide a useful reference for future studies. Moreover, the elastic stability criterion for orthorhombic crystals under isotropic pressure is as follows [33,34]:

$$\begin{aligned} C_{ii} > 0 (i = 1, 4, 5, 6), \quad C_{11}C_{22} - C_{12}^2 > 0, \\ C_{11}C_{22}C_{33} + 2C_{12}C_{13}C_{23} - C_{11}C_{23}^2 - C_{22}C_{13}^2 - C_{33}C_{12}^2 > 0, \end{aligned} \quad (12)$$

It is obvious that the theoretical elastic constants of the orthorhombic TiAl under different pressure can satisfy the elastic stability criterion, making the orthorhombic cell mechanically stable. To ensure the stability of the orthorhombic TiAl, the phonon spectra are calculated at 0 GPa and 100 GPa (see Figure 3). There are no imaginary frequencies, indicating that the orthorhombic TiAl can be stable up to 100 GPa.

**Table 2.** The elastic constants  $C_{ij}$  (in GPa) of the orthorhombic TiAl under pressure up to 100 GPa.

$P$	$C_{11}$	$C_{12}$	$C_{13}$	$C_{22}$	$C_{23}$	$C_{33}$	$C_{44}$	$C_{55}$	$C_{66}$
0	206.90	68.03	47.40	193.56	79.65	218.56	56.15	54.17	74.66
10	260.12	83.71	61.45	239.30	104.51	267.14	65.40	67.95	91.45
20	309.50	99.74	72.87	279.31	127.09	305.42	73.06	79.20	105.55
30	355.40	116.64	81.78	309.93	152.57	336.49	78.80	86.60	118.61
40	399.59	130.41	93.43	340.45	174.01	368.51	85.28	92.50	130.20
50	441.64	141.36	105.53	371.18	192.30	402.62	92.01	98.05	140.47
60	482.66	154.15	114.05	403.73	209.87	432.78	95.75	100.53	150.48
70	518.99	165.85	124.43	430.46	229.20	462.66	97.52	103.41	158.18
80	552.09	178.17	135.87	454.08	247.04	484.82	97.05	105.24	165.41
90	581.41	188.91	151.06	472.70	263.88	504.37	94.58	105.97	172.14
100	610.47	200.27	164.36	492.73	279.07	514.74	94.00	105.66	178.59

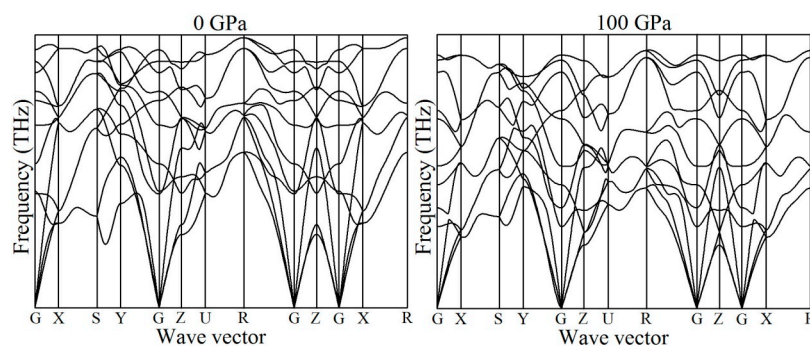


**Figure 3.** The phonon spectra of the orthorhombic TiAl at 0 GPa and 100 GPa.

Table 3 lists the calculated results of the bulk modulus  $B$ , shear modulus  $G$ , Young's modulus  $E$ , and Poisson ratio  $\nu$  of the orthorhombic TiAl under pressure up to 100 GPa. It is obvious that each of  $B$ ,  $G$ ,  $E$ , and  $\nu$  increases with increasing pressure. The bulk modulus ( $B_{eq}$ ) obtained using a Birch–Murnaghan equation of state (EOS) fitting the volume–energy data at a given pressure is also listed in Table 3 for comparison [35]. The EOS-fitted bulk modulus is in excellent agreement with the value obtained from elastic calculations. The zero-pressure bulk modulus of the orthorhombic TiAl is very close to that of pure  $\alpha$ -Ti ( $117 \pm 9$  GPa) [36], but is significantly larger than that of pure Al

(73 GPa) [37]. Additionally, the zero pressure bulk modulus of the orthorhombic TiAl falls within the range of  $97 \pm 3$  GPa to  $124 \pm 6$  GPa for  $\beta$ -Ti-based alloys [38].

**Table 3.** The Voigt, Reuss, Hill, and bulk ( $B_V$ ,  $B_R$ ,  $B$ ,  $B_{eq}$ , in GPa) and shear ( $G_V$ ,  $G_R$ ,  $G$  in GPa) moduli, Young's modulus ( $E$  in GPa), Poisson ratio ( $\nu$ ), and Vickers hardness ( $H_V$  in GPa) of the orthorhombic TiAl under pressure up to 100 GPa.

$P$	$B_V$	$B_R$	$B$	$B_{eq}$	$G_V$	$G_R$	$G$	$G/B$	$E$	$\nu$	$H_V$
0	112.13	111.92	112.02	112.39	65.26	63.41	64.33	0.574	161.99	0.259	8.936
10	140.66	140.42	140.54	140.08	79.42	76.95	78.18	0.556	197.86	0.265	9.889
20	165.96	165.77	165.87	165.68	91.20	87.96	89.58	0.540	227.73	0.271	10.489
30	189.31	189.14	189.23	188.60	100.19	95.54	97.87	0.517	250.43	0.279	10.500
40	211.58	211.47	211.53	211.41	108.98	103.26	106.12	0.502	272.75	0.285	10.675
50	232.64	232.59	232.62	231.84	117.86	111.37	114.61	0.493	295.33	0.288	11.006
60	252.81	252.75	252.78	251.99	125.43	117.59	121.51	0.481	314.18	0.293	11.081
70	272.34	272.29	272.31	270.15	131.33	122.12	126.73	0.465	329.13	0.299	10.872
80	290.34	290.29	290.32	287.69	135.53	124.83	130.18	0.448	339.75	0.305	10.491
90	307.35	307.34	307.35	306.74	138.18	125.87	132.03	0.430	346.47	0.312	9.965
100	322.82	322.76	322.79	324.27	140.60	126.84	133.72	0.414	352.48	0.318	9.495

As suggested by Pugh [39], a material behaves in a ductile manner if  $G/B < 0.5$ , otherwise it should be brittle. It is clear that the  $G/B$  ratio decreases with increasing pressure and has a value of 0.517 at 30 GPa and 0.502 at 40 GPa. According to Frantsevich's rule [40], a material is brittle if its Poisson's ratio is less than  $1/3$ ; otherwise, the material is ductile. It is seen that the Poisson's ratio increases from 0.259 to 0.318 with increasing pressure. As suggested by Pettifor [41], a material has more metallic (angular) bonds and is thus more ductile (brittle) if it has a larger positive (negative) Cauchy pressure. For an orthorhombic crystal, the Cauchy pressures can be defined as  $C_{23}-C_{44}$  for (100) plane,  $C_{13}-C_{55}$  for (010) plane, and  $C_{12}-C_{66}$  for (001) plane. Figure 4 shows the pressure-dependent Cauchy pressures of the orthorhombic TiAl. In Figure 4a, the positive value of  $C_{23}-C_{44}$  is always large and increases with increasing pressure. In Figure 4b, the values of  $C_{13}-C_{55}$  and  $C_{12}-C_{66}$  also increase on the whole with increasing pressure. At 30 and 40 GPa, the values of  $C_{13}-C_{55}$  correspond to  $-4.826$  and  $0.928$  GPa, and those of  $C_{12}-C_{66}$  correspond to  $-1.972$  and  $0.205$  GPa. These show that the orthorhombic TiAl has intrinsic brittleness at pressures smaller than 40 GPa while having intrinsic ductility under higher pressure. Moreover, the Vickers hardness of materials can be expressed as  $H_V = 2(k^2G)^{0.585} - 3$ , where  $k = G/B$  [42–44]. The calculated values of Vickers hardness for the orthorhombic TiAl under pressure up to 100 GPa are also listed in Table 3. It is observed that the Vickers hardness firstly increases from 8.936 GPa and then starts to decrease from 11.081 GPa to 9.495 GPa after 60 GPa.

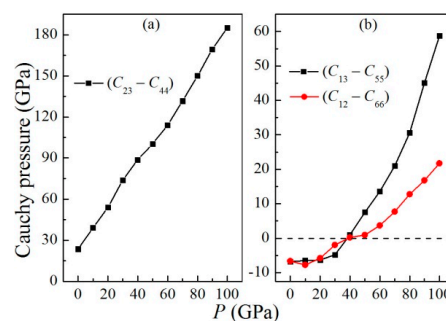


**Figure 4.** The pressure dependence of the Cauchy pressures (a)  $C_{23}-C_{44}$ , (b)  $C_{13}-C_{55}$ , and  $C_{12}-C_{66}$  of the orthorhombic TiAl.

Figure 5 shows the calculated results of various anisotropy factors under pressure up to 100 GPa. In Figure 5a, as the pressure increases, the value of  $A_{\{100\}}$  decreases monotonously from 0.6793,  $A_{\{010\}}$

firstly increases quickly from 0.8571 and starts to decrease slowly from 1.0251 after 40 GPa, and  $A_{\{001\}}$  decreases slowly on the whole from 1.1295 to 1.0167.  $A_{\{100\}}$  has the largest absolute deviation from one under identical pressure, indicating that the shear anisotropy for the {100} plane is the strongest. The difference of these shear anisotropy factors is due to the variations of the elastic constants with the pressure. In Figure 5b, as the pressure increases, the positive value of  $A_B$  decreases very slowly from 0.0945%, and  $A_G$  increases sharply from 1.4370% to 5.1436%. Under identical pressure, the value of  $A_G$  is significantly larger than the corresponding one of  $A_B$ . These imply that the anisotropy in shear is stronger than the corresponding one in compressibility. However, the above anisotropy measures ignore the bulk contributions of the elastic stiffness tensor. The universal anisotropy index  $A^U$  can overcome the limitations. It is clear that the positive value of  $A^U$  increases with increasing pressure, indicating that the elastic anisotropy of the orthorhombic TiAl increases with increasing pressure.

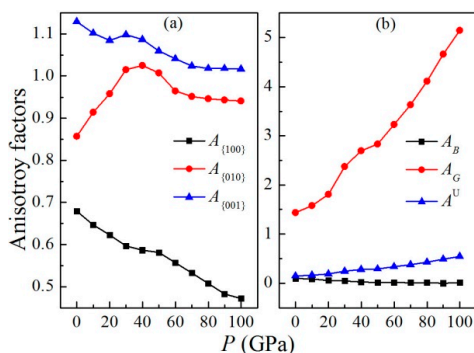


**Figure 5.** The pressure dependence of the shear anisotropy factors ( $A_{\{100\}}$ ,  $A_{\{010\}}$  (a), and  $A_{\{001\}}$ ), percent anisotropy factors of bulk ( $A_B$ ) and shear ( $A_G$ ) moduli, and universal anisotropy factor ( $A^U$ ) of the orthorhombic TiAl (b).

Table 4 gives the pressure dependence of the mass density, transverse, longitudinal, and average sound velocities, and Debye temperature of the orthorhombic TiAl. It can be found that as the pressure increases, the density  $\rho$  increases monotonously, the transverse sound velocity  $V_t$  firstly increases from 4098.8 m/s and then starts to decrease from 4876.6 m/s to 4815.2 m/s after 70 GPa, and the longitudinal sound velocity  $V_l$  increases monotonously from 7187.0 m/s to 9321.1 m/s. Because of the pressure effect on the transverse and longitudinal sound velocities, the average sound velocity  $V_m$  firstly increases from 4555.2 m/s and then starts to decrease from 5447.0 m/s to 5390.9 m/s after 80 GPa. It can also be found that the Debye temperature increases with increasing pressure.

**Table 4.** The density ( $\rho$  in g/cm<sup>3</sup>), transverse ( $V_t$ ), longitudinal ( $V_l$ ), and average ( $V_m$ ) elastic wave velocities (in m/s) and Debye temperature ( $\Theta_D$  in K) of the orthorhombic TiAl under pressure up to 100 GPa.

$P$	$\rho$	$V_t$	$V_l$	$V_m$	$\Theta_D$
0	3.8295	4098.8	7187.0	4555.2	535.50
10	4.1342	4348.7	7694.7	4836.7	583.29
20	4.4531	4485.1	8004.2	4991.8	617.09
30	4.6106	4607.2	8327.3	5133.0	641.94
40	4.8113	4696.4	8565.8	5236.0	664.19
50	4.9962	4789.6	8783.3	5342.1	686.22
60	5.1670	4849.3	8959.8	5411.7	702.99
70	5.3290	4876.6	9099.9	5446.0	714.77
80	5.4810	4873.5	9199.7	5447.0	721.63
90	5.6266	4844.0	9268.8	5419.1	724.23
100	5.7673	4815.2	9321.1	5390.9	726.42

#### 4. Conclusions

The structural and elastic properties of the orthorhombic TiAl under pressure up to 100 GPa have been obtained by the first-principles density functional theory calculations based on the projector augmented wave and the generalized gradient approximation. The equilibrium lattice parameters at 0 GPa are found to be in agreement with the available experimental data. The pressure dependence of the elastic constants, elastic moduli, Poisson's ratio, Cauchy pressure, elastic anisotropy, and Debye temperature are investigated for the first time. By the elastic stability criterion under isotropic pressure, it is found that the orthorhombic TiAl is mechanically stable under pressure up to 100 GPa. By analyzing the Pugh's ratio, Cauchy pressure, and Poisson's ratio, the ductile/brittle behavior of the orthorhombic TiAl is evaluated. It is shown that the ductility of the orthorhombic TiAl increases with increasing pressure and a brittle-to-ductile transition occurs at 40 GPa. Besides, the elastic anisotropy and Debye temperature of the orthorhombic TiAl are found to increase with increasing pressure. Although there is no available experimental and theoretical data under pressure for comparison, the present results can provide a useful reference for future experimental and theoretical works.

**Acknowledgments:** The work is supported by the Scientific and Technological Research Program of Chongqing Municipal Education Commission (KJ1710252), the Natural Science Foundation of China (11104361), Project supported by Program for Innovation Team Building at Institutions of Higher Education in Chongqing (CXTDX201601034).

**Author Contributions:** Rui Wang, Yelu He and Xing Zou performed the theoretical calculations; Lili Liu, Xiaozhi Wu and Xiangfei Nie analyzed the theoretical data; Lili Liu wrote the paper.

**Conflicts of Interest:** The authors declare no conflict of interest.

#### References

1. Kestler, H.; Clemens, H. Production, Processing and Application of  $\gamma$ (TiAl)-Based Alloys. In *Titanium and Titanium Alloys*; Leyens, C., Peters, M., Eds.; Wiley-VCH: Weinheim, Germany, 2003; p. 351.
2. Abe, E.; Kumagai, T.; Nakamura, M. New ordered structure of TiAl studied by high-resolution electron microscopy. *Intermetallics* **1996**, *4*, 327–333. [[CrossRef](#)]
3. Appel, F.; Oehring, M.; Paul, J.D.H. Nano-scale design of TiAl alloys based on  $\beta$ -phase decomposition. *Adv. Eng. Mater.* **2006**, *8*, 371–376. [[CrossRef](#)]
4. Tanimura, M.; Inoue, Y.; Koyama, Y. Change in Al concentration profile related to the  $D0_{19} \rightarrow L1_0$  structural change in Ti-Al alloys. *Scr. Mater.* **2001**, *44*, 365–373. [[CrossRef](#)]
5. Ducher, R.; Viguier, B.; Lacaze, J. Modification of the crystallographic structure of  $\gamma$ -TiAl alloyed with iron. *Scr. Mater.* **2002**, *47*, 307–313. [[CrossRef](#)]
6. Schmoelzer, T.; Stark, A.; Schwaighofer, E.; Lippmann, T.; Mayer, S.; Clemens, H. In situ synchrotron study of B19 phase formation in an intermetallic  $\gamma$ -TiAl alloys. *Adv. Eng. Mater.* **2012**, *14*, 445–448. [[CrossRef](#)]
7. Song, L.; Xu, X.J.; You, L.; Liang, Y.F.; Lin, J.P. B19 phase in Ti-45Al-8.5Nb-0.2W-0.2B-0.02Y alloy. *J. Alloys Compd.* **2015**, *618*, 305–310. [[CrossRef](#)]
8. Nguyen-Manh, D.; Pettifor, D.G. Electronic structure, phase stability and elastic moduli of AB transition metal aluminides. *Intermetallics* **1999**, *7*, 1095–1106. [[CrossRef](#)]
9. Nguyen-Manh, D.; Pettifor, D.G. Origin of O-Phase and Pseudo-Twinning in Ti-Al-Nb Alloys: A First-Principles Study. In *Gamma Titanium Aluminides*; Kim, Y.-W., Dimiduk, D.M., Loretto, M.H., Eds.; TMS: Warrendale, PA, USA, 1999; pp. 175–182.
10. Holec, D.; Reddy, R.K.; Klein, T.; Clemens, H. Preferential site occupancy of alloying elements in TiAl-based phases. *J. Appl. Phys.* **2016**, *119*, 339–341. [[CrossRef](#)]
11. Wen, Y.; Wang, L.; Liu, H.; Song, L. Ab initio study of the elastic and mechanical properties of B19 TiAl. *Crystals* **2017**, *7*, 39–49. [[CrossRef](#)]
12. Blöchl, P.E. Projector augmented-wave method. *Phys. Rev. B* **1994**, *50*, 17953–17979. [[CrossRef](#)]
13. Perdew, J.P.; Burke, K.; Ernzerhof, M. Generalized gradient approximation made simple. *Phys. Rev. Lett.* **1996**, *77*, 3865–3868. [[CrossRef](#)] [[PubMed](#)]
14. Perdew, J.P.; Burke, K.; Ernzerhof, M. Generalized gradient approximation made simple. *Phys. Rev. Lett.* **1997**, *78*, 1396. [[CrossRef](#)]

15. Kresse, G.; Furthmüller, J. Efficiency of ab-initio total energy calculations for metals and semiconductors using a plane-wave basis set. *Comput. Mater. Sci.* **1996**, *6*, 15–150. [[CrossRef](#)]
16. Kresse, G.; Furthmüller, J. Efficient iterative schemes for ab initio total-energy calculations using a plane-wave basis set. *Phys. Rev. B* **1996**, *54*, 11169–11186. [[CrossRef](#)]
17. Kresse, G.; Joubert, D. From ultrasoft pseudopotentials to the projector augmented-wave method. *Phys. Rev. B* **1999**, *59*, 1758–1775. [[CrossRef](#)]
18. Monkhorst, H.J.; Pack, J.D. Special points for Brillouin-zone integrations. *Phys. Rev. B* **1976**, *13*, 5188–5192. [[CrossRef](#)]
19. Le Page, Y.; Saxe, P. Symmetry-general least-squares extraction of elastic data for strained materials from ab initio calculations of stress. *Phys. Rev. B* **2002**, *65*, 104104–104117. [[CrossRef](#)]
20. Wu, X.; Vanderbilt, D.; Hamann, D.R. Systematic treatment of displacements, and electric fields in density-functional perturbation theory. *Phys. Rev. B* **2005**, *72*, 035105–035117. [[CrossRef](#)]
21. Hamann, D.R.; Wu, X.; Rabe, K.M.; Vanderbilt, D. Metric tensor formulation of strain in density-functional perturbation theory. *Phys. Rev. B* **2005**, *71*, 035117. [[CrossRef](#)]
22. Erba, A. The internal-strain tensor of crystals for nuclear-relaxed elastic and piezoelectric constants: On the full exploitation of its symmetry features. *Phys. Chem. Chem. Phys.* **2016**, *18*, 13984–13992. [[CrossRef](#)] [[PubMed](#)]
23. Erba, A.; Caglioti, D.; Dovesi, R. Nuclear-relaxed elastic and piezoelectric constants of materials: Computational aspects of two quantum-mechanical approaches. *J. Comput. Chem.* **2017**, *38*, 257–264. [[CrossRef](#)] [[PubMed](#)]
24. Hill, R. The elastic behaviour of a crystalline aggregate. *Proc. Phys. Soc. A* **1953**, *65*, 349–354. [[CrossRef](#)]
25. Voigt, W. *Lehrbuch der Kristallphysik*; Teubner: Leipzig, Germany, 1928.
26. Reuss, A.; Angew, Z. Berechnung der fließgrenze von mischkristallen auf grund der plastizitätsbedingung für einkristalle. *Math. Mech.* **1929**, *9*, 49–58.
27. Ravindran, P.; Fast, L.; Korzhavyi, P.A.; Johansson, B.; Wills, J.; Eriksson, O. Density functional theory for calculation of elastic properties of orthorhombic crystals: Application to TiSi<sub>2</sub>. *J. Appl. Phys.* **1998**, *84*, 4891–4904. [[CrossRef](#)]
28. Chung, D.H.; Buessem, W.R. The elastic anisotropy of crystals. *J. Appl. Phys.* **1967**, *38*, 2010–2012. [[CrossRef](#)]
29. Ranganathan, S.I.; Ostoja-Starzewski, M. Universal elastic anisotropy index. *Phys. Rev. Lett.* **2008**, *101*, 055504–055507. [[CrossRef](#)] [[PubMed](#)]
30. Anderson, O.L. A simplified method for calculating the Debye temperature from elastic constants. *J. Phys. Chem. Solids* **1963**, *24*, 909–917. [[CrossRef](#)]
31. Schreiber, E.; Anderson, O.L.; Soga, N. *Elastic Constants and Their Measurements*; McGraw-Hill: New York, NY, USA, 1973.
32. Erba, A.; Mahmoud, A.; Belmonte, D.; Dovesi, R. High pressure elastic properties of minerals from ab initio simulations: The case of pyrope, grossular and andradite silicate garnets. *J. Chem. Phys.* **2014**, *140*, 124703. [[CrossRef](#)] [[PubMed](#)]
33. Mouhat, F.; Coudert, F.X. Necessary and sufficient elastic stability conditions in various crystal systems. *Phys. Rev. B* **2014**, *90*, 224104. [[CrossRef](#)]
34. Chang, J.; Chen, X.R.; Wei, D.Q.; Yuan, X.L. Elastic constants and anisotropy of  $\beta$ -BC<sub>2</sub>N under pressure. *Physica B* **2010**, *405*, 3751–3755. [[CrossRef](#)]
35. Birch, F. Finite elastic strain of cubic crystals. *Phys. Rev.* **1947**, *71*, 809–824. [[CrossRef](#)]
36. Errandonea, D.; Meng, Y.; Somayazulu, M.; Hausermann, D. Pressure-induced  $\alpha \rightarrow \omega$  transition in titanium metal: A systematic study of the effects of uniaxial stress. *Phys. B* **2005**, *355*, 116–125. [[CrossRef](#)]
37. Dewaele, A.; Loubeyre, P.; Mezouar, M. Equations of state of six metals above 94 GPa. *Phys. Rev. B* **2004**, *70*, 094112. [[CrossRef](#)]
38. Smith, D.; Joris, O.P.J.; Sankaran, A.; Weekes, H.E.; Bull, D.J.; Prior, T.J.; Dye, D.; Errandonea, D.; Proctor, J.E. On the high-pressure phase stability and elastic properties of  $\beta$ -titanium alloys. *J. Phys. Condens. Matter* **2017**, *29*, 155401. [[CrossRef](#)] [[PubMed](#)]
39. Pugh, S.F. Relations between the elastic moduli and the plastic properties of polycrystalline pure metals. *Philos. Mag.* **1954**, *45*, 823–843. [[CrossRef](#)]
40. Frantsevich, I.N.; Voronov, F.F.; Bokuta, S.A. *Elastic Constants and Elastic Moduli of Metals and Insulators Handbook*; Frantsevich, I.N., Ed.; Naukova Dumka: Kiev, Ukraine, 1983; pp. 60–180.

41. Pettifor, D. Theoretical predictions of structure and related properties of intermetallics. *Mater. Sci. Technol.* **1992**, *8*, 345–349. [[CrossRef](#)]
42. Teter, D.M. Computational alchemy: The search for new superhard materials. *MRS Bull.* **1998**, *23*, 22–27. [[CrossRef](#)]
43. Errandonea, D.; Ferrer-Roca, C.; Martinez-Carcia, D.; Segura, A.; Gomis, O.; Munoz, A.; Rodriguez-Hernandez, P.; Lopez-Solnano, J.; Alconchel, S.; Sapina, F. High-pressure X-ray diffraction and ab initio study of Ni<sub>2</sub>Mo<sub>3</sub>N, Pd<sub>2</sub>Mo<sub>3</sub>N, Pt<sub>2</sub>Mo<sub>3</sub>N, Co<sub>3</sub>Mo<sub>3</sub>N, and Fe<sub>3</sub>Mo<sub>3</sub>N: Two families of ultra-incompressible bimetallic interstitial nitrides. *Phys. Rev. B* **2010**, *82*, 174105. [[CrossRef](#)]
44. Liu, L.L.; Xu, G.; Wang, A.R.; Wu, X.Z.; Wang, R. First-principles investigations on structure stability, elastic properties, anisotropy and Debye temperature of tetragonal LiFeAs and NaFeAs under pressure. *J. Phys. Chem. Solids* **2017**, *104*, 243–251. [[CrossRef](#)]



© 2017 by the authors. Licensee MDPI, Basel, Switzerland. This article is an open access article distributed under the terms and conditions of the Creative Commons Attribution (CC BY) license (<http://creativecommons.org/licenses/by/4.0/>).